

Sense and non-sense of shear reloaded

Bernhard Grasemann¹, Marcin Dabrowski^{2,3}, Martin P.J. Schöpfer¹

¹ Department for Geodynamics and Sedimentology, University of Vienna, Austria (Bernhard.Grasemann@univie.ac.at)

² Computational Geology Laboratory, Polish Geological Institute - National Research Institute, Wroclaw, Poland

³ Physics of Geological Processes (PGP), The NJORD Centre,, University of Oslo, Norway

Abstract

This paper reviews the geometrical and mechanical evolution of selected groups of kinematic indicators that are frequently used for inferring large-scale geodynamics but are prone to ambiguous shear sense interpretations: (i) Flanking folds and shear bands are complex structures because under general shear conditions co-rotating secondary shear zones can experience either syn- or antithetic slip leading to extensional or contractional offsets. On the other hand, counter-rotating secondary shear zones can exhibit either extensional or contractional offsets but always experience synthetic slip. (ii) Boudinaged layers may display both syn- and antithetic offset across the interboudin surfaces. In addition to the flow type, the initial orientation of interboudin surfaces strongly influences the sense of slip. Under coaxial flow conditions and with high-strength contrast between the boudinaged layer and the matrix, domains of layer-oblique parallel interboudin surfaces can form by chance and their local occurrence may hence lead to misinterpretations of shear zone kinematics, in particular if the number of observable boudins is small. If the viscosity contrast between the boudinaged layer and the matrix is low, domino boudins may strongly deform internally during shearing so that, in contrast to flanking structures, antithetic slip along interboudin surface may lead to a marked normal drag, resulting in shear band boudinage geometries that appear to have formed during flow with an opposite shear sense. (iii) Winged inclusions are pinch-and-swell shaped objects rotating into the shear direction. After several revolutions, these structures can resemble σ_b -type clasts or clasts with stair stepping that formed during shear flow with the opposite shear sense. In this paper, new and published examples of these ambiguous shear sense indicators are discussed and interpreted. We give some guidelines for the correct interpretation of these structures with the caveat that if marker lines and their deflections are not well-preserved these shear sense criteria are not always reliable kinematic indicators.

30 1. Introduction

31 One of the major aim in tectonic studies is to derive the progressive kinematic history recorded in
32 sheared rocks, in particular when these rocks define boundaries between different tectono-
33 metamorphic units. Before the launch of the *Journal of Structural Geology* in 1979, kinematic
34 interpretations of faults and shear zones in structural geology textbooks were mainly restricted to offset
35 marker horizons and fold vergence (Turner and Weiss, 1963; de Sitter, 1964; Billings, 1972; Hills, 1972).
36 With notable exceptions, kinematic interpretations in these textbooks focused on tension and shear
37 fractures in brittle faults (Hills, 1972), oblique fabrics (Sander, 1950), or rotated minerals in sheared
38 metamorphic rocks (Fairbairn, 1949).

39 As the interest in physical concepts of flow and progressive deformation in structural geology
40 increased (e.g. Elliot, 1972; Ramberg, 1975; Ghosh and Ramberg, 1976; Means et al., 1980; Lister and
41 Williams, 1979; Passchier, 1986, 1988), several new kinematic indicators were described and
42 summarized in seminal review papers on shear sense indicators in brittle and ductile rocks (Petit, 1987;
43 Passchier and Simpson, 1986; White et al., 1986, Hanmer and Passchier, 1991). Quantitative
44 measurements of orientations and finite strain preserved in structures with monoclinic symmetry were
45 used to derive the kinematic vorticity number (for a review see Xypolias, 2010 and references cited
46 therein), which is a measure of the ratio of the pure and simple shear component of the flow (Means et
47 al., 1980). Modern structural geology textbooks provide comprehensive overviews of kinematic
48 indicators in brittle faults and ductile shear zones (e.g. Blenkinsop, 2000; van der Pluijm and Marshak,
49 2004; Passchier and Trouw, 2005; Twiss and Moores, 2007; Fossen, 2016), giving the impression that the
50 interpretation of the “shear sense” is straightforward and well understood.

51 However, detailed field observations (e.g. Simpson and Schmid, 1983; Behrmann, 1987; Hanmer and
52 Passchier, 1991; Passchier and Williams, 1996) and in particular results of analytical and numerical
53 models (e.g. Mandal et al., 2000a; Passchier and Druguet, 2002; Samanta et al., 2002; Schmid and
54 Podladchikov, 2004; Kocher and Mancktelow, 2005; Mulchrone et al., 2005; Wiesmayr and Grasemann,
55 2005; Jiang, 2007; Fletcher, 2009; Dabrowski and Schmid, 2011; Schmalholz and Maeder, 2012;
56 Dabrowski and Grasemann, 2014; Marques et al., 2014; Grasemann and Dabrowski, 2015; Adamuszek
57 and Dabrowski, 2017; Schöpfer et al., 2017) challenged some of the classical interpretations of structures
58 with monoclinic symmetries because the strain evolution of kinematic indicators can be significantly
59 influenced by numerous factors, such as mechanical interactions, confined flow, slipping interfaces,
60 initial geometrical configurations, composite rheological materials and mechanical anisotropies. In this
61 review, we focus on a selection of frequently used groups of kinematic indicators, in particular flanking

62 structures, boudinage and rotating inclusions in ductile shear zones, which may lead to ambiguous
63 interpretations of the shear sense. Our interpretation of these structures is supported by the results of
64 mechanical models, which assist in identifying well-preserved natural examples. The paper concludes
65 with a discussion of selected natural examples, some of which are published but allow alternative
66 interpretations.

67

68 2. Ambiguous shear sense criteria

69 2.1. Flanking structures developed along secondary shear zones

70 Secondary shear zones known as shear bands, *C'*-type or extensional crenulation cleavage have been
71 recognized to record important information about the kinematic history of sheared rocks (Berthé et al.,
72 1979; White, 1979; Platt and Vissers, 1980). In fact, shear bands are one particular geometry, and various
73 other geometries can develop along cross cutting elements or slip surfaces that localize deformation,
74 leading to a large family of structures collectively called flanking structures (Grasemann and Stüwe,
75 2001; Passchier, 2001). Flanking structures can be classified on the basis of their sense of slip (syn- or
76 antithetic) and their drag geometry (normal or reverse; Wiesmayr and Grasemann, 2005). A non-generic
77 classification based on geometric criteria developed around secondary shear zones has been suggested
78 by Coelho et al. (2005). Under the simplest circumstances, namely two-dimensional uniform general
79 shear of homogenous and anisotropic materials, these secondary shear zones generally have the
80 rotational behaviour of passive marker lines in a homogeneous medium (Kocher and Mancktelow, 2005)
81 and their instantaneous rotation rate, stretch and shear are primarily dependent on their orientation and
82 the kinematic vorticity number of the flow. Figure 1 shows an off-axis Mohr Circle representation of the
83 deformation gradient tensor F (De Paor and Means, 1984) showing the eigenvectors of flow ($a_{1,2}$), the
84 angle α between the eigenvectors, the instantaneous stretching axes ($ISA_{1,2}$), and the maximum and
85 minimum shear strain rate ($\dot{\gamma}_{1,2}$). The lower right (F_{11}, F_{21}) and the upper left coordinates (F_{12}, F_{22}) of the
86 deformed unit square correspond to the components of F . If there is no shear component perpendicular
87 to the base of the unit square (i.e. $F_{21} = 0$) the kinematic vorticity number W_k (e.g. Means et al., 1980),
88 which is the cosine of α , can be simply expressed by the components of F by

89
$$W_k = \frac{1}{\sqrt{\left(\frac{F_{11}-F_{22}}{F_{12}}\right)^2 + 1}}. \quad (1)$$

90 Under simple shear all material lines rotate into the shear direction (Fig. 1a), but under general shear
91 (Fig. 1b) counter-rotation also occurs, resulting in six different behavioural fields for secondary finite
92 shear zones (Grasemann et al., 2003): Co-rotating shear zones can either experience synthetic
93 slip/shortening (+I), antithetic slip/shortening (+II), antithetic slip/stretching (+III), or synthetic
94 slip/stretching (+IV). Counter-rotating material lines can only experience synthetic slip and are either
95 shortening (-I) or stretching (-II). For geometrical reasons, a central marker line offset by the secondary
96 shear zone will always exhibit reverse drag (Coelho et al., 2005) that may be superposed by normal drag
97 (Grasemann et al., 2005), resulting in a number of instantaneous flanking structure geometries that may
98 record approximate mirror symmetries between the end-member deformations of pure shear
99 transtension, simple shear and pure shear transpression (Wiesmayr and Grasemann, 2005). The
100 progressive development of flanking structures during large strain deformation is even more complex
101 since the secondary shear zone might rotate through the different fields and hence can switch slip from
102 syn- to antithetic and back to synthetic (Exner et al., 2004, Kocher and Mancktelow, 2005; see movie in
103 DR 1). In general shear transpression and transtension, under which secondary shear zones might also
104 experience back-rotation, similar mirror-imaged structures may develop hampering their kinematic
105 interpretation (Wiesmayr and Grasemann, 2005). For example, synthetic shear bands with a central
106 marker line exhibiting reverse drag resemble mirror images of extensional flanking structures that
107 developed along antithetic secondary shear zones (compare Fig. 2a and b). Similarly, flanking structures
108 exhibiting contractional offset of a central marker along an antithetic secondary shear zone mimic the
109 mirror symmetry of structures formed along synthetic secondary shear zones (compare Fig. 2c and d).
110 However, a closer inspection of Figure 2 provides clues that help discriminating these structures, a task
111 that is attainable when the inspected natural example shows clearly visible marker lines:

112 Under general shear, synthetic shear bands develop parallel to the shortening flow eigenvector (Fig. 2a)
113 and do not rotate into the shear direction. During ongoing deformation the shear bands accumulate
114 synthetic slip that displaces, within the shortening quadrants, the central marker line with increasing
115 shearing towards the secondary shear zone tips, resulting in a marked reverse drag. On the other hand,
116 within the extensional quadrants, the marker lines are deformed to become almost parallel to the
117 secondary shear zone, resulting in a marked normal drag. This change from normal to reverse drag along
118 the secondary shear zone results in peculiar geometries exhibiting marker lines at both zone ends that
119 meet at almost right angles.

120 Extensional flanking structures developing along antithetic secondary shear zones (Fig. 2b) can never
121 accumulate an offset as large as synthetic shear bands, because they rotate at some stage (in simple

122 shear but also in general shear) into the field where the marker's offset along the secondary shear zones
123 switches from anti- to synthetic. The resulting normal drag in the extensional quadrants of the secondary
124 shear zone may become less pronounced, but the reverse drag in the compressional quadrants is
125 frequently characterized by markers with a prominent hook-shape (Hudleston, 1989) or over-roll (Coelho
126 et al., 2005). In summary, synthetic shear bands and extensional flanking structures developing along
127 antithetic secondary shear zones may be difficult to discriminate except for large offset at the tip of the
128 secondary shear zone, a feature that is however only typical for synthetic shear bands.

129 In simple shear contractional synthetic and antithetic flanking structures can be distinguished by the
130 acute angle between the secondary shear zone and the shear zone boundary like so: Contractional
131 synthetic flanking structures have acute angles smaller than 45° , whereas contractional antithetic
132 flanking structures have acute angles greater than 45° (Fig. 2c and d). However, distinction between
133 these two types of flanking structures is difficult or even impossible under general shear, or when
134 markers are initially oblique to the shear zone boundary, or when the orientation of the shear zone
135 boundary is uncertain (Grasemann and Wiesmayr, 2005).

136 2.2. Domino and shear band boudinage

137 In monoclinic shear zones layer boudinage can be classified into three end member classes with respect
138 to the bulk shear sense: (i) symmetric boudinage without slip on the inter-boudin surface (no-slip
139 boudinage); (ii) synthetic (shear band) boudinage or (iii) antithetic (domino) boudinage (for more details
140 and subdivisions including the boudin shapes based on more than 2000 natural examples see Goscombe
141 et al., 2004). However, the kinematic interpretation of boudinage is not always straightforward and
142 requires knowledge of the initial orientation of the interboudin surfaces with respect to both the
143 boudinaged layer and the shear zone boundary (Passchier and Druguet, 2002; Goscomb and Passchier,
144 2003; Mandal et al., 2007). Dependent on elastic properties, strength and mechanical anisotropy of the
145 surrounding material (Strömgård, 1973; Mandal et al., 2000b; Mancktelow, 2008), boudin trains develop
146 interboudin surfaces approximately perpendicular to layering, forming either torn, which are frequently
147 reworked into domino boudinage (Goscombe et al., 2004). Alternatively, boudin trains may develop
148 backward or forward vergent interboudin surfaces with syn- and antithetic slip, resulting in shear band
149 boudinage with mirror symmetries (Goscombe and Passchier, 2003). As a consequence the final
150 boudinage structure is strongly dependent on the initial orientation of the interboudin surfaces with
151 respect to the boudinaged layer.

152 Numerical models and natural examples suggest that, besides the symmetric boudinage without
153 slip on the inter-boudin surfaces, also symmetric shear fracture boudinage (“horst and graben
154 structure”) with backward- and forward vergent interboudin surfaces may develop, resulting in
155 geometries typically interpreted to have formed under coaxial strain boundary conditions (e.g. Schenk et
156 al., 2007; Abe and Urai, 2011; Schöpfer et al., 2017). A quantitative measure of the relative amount of
157 extension accommodated by oppositely dipping interboudin surfaces is the polarity ($-1 \leq P \leq 1$), defined
158 as the normalized sum of throw T on left dipping (positive throw) and on right dipping (negative throw)
159 surfaces, i.e. $P = \sum T / |\sum T|$ (alternatively the signed heave can be taken). Absolute polarity values close to
160 one are hence characteristic for asymmetric boudinage (typically interpreted to have formed under
161 non-coaxial flow), whereas symmetric fracture boudinage yields values of around zero (likely to reflect
162 co-axial flow). Numerical models (see Appendix A.2. for details) of fracture boudinage formation under
163 coaxial boundary conditions revealed however that the ‘classical interpretation’ of asymmetric shear
164 band boudinage may be incorrect, because parallel layer-oblique interboudin surface can form by
165 chance, in particular when the strength contrast between the boudinaged layer and the surrounding
166 material is high so that the boudins can rotate during progressive deformation (Schöpfer et al, 2017).
167 Figure 3 shows the results of three discrete element method (DEM) models (for model details see
168 Appendix A.2. and Schöpfer et al, 2017) of the formation of fracture boudinage under coaxial strain
169 boundary conditions after 10% extension. The three results started all with the same initial geometry
170 and identical particle/bond properties, but different random placement of particles, comprising a central
171 brittle layer (with passive markers) embedded in a weak matrix. The local presence of parallel layer-
172 oblique interboudin surface may hence not reflect a non-coaxial background flow, in particular when the
173 sample size (e.g., number of boudins) is small, because if the dip direction of the interboudin surfaces is
174 random and independent of the adjacent surfaces, the probability p for N surfaces dipping in the same
175 direction is $p = (1/2)^{(N-1)}$ (e.g., there is a 25% chance for three parallel surfaces; Schöpfer et al, 2017). A
176 simple probability analysis could help to assess whether the number of interboudin surfaces is large
177 enough to draw kinematic conclusions about the polarity of asymmetric boudinage.

178 The mechanical evolution of deformable domino boudinage is even more complex because the
179 angle between the interboudin surface and the boudin layer boundary (i.e. the enveloping surface) may
180 change during progressive non-coaxial deformation (Dabrowski and Grasemann, 2014). Therefore,
181 deformable domino boudins have been compared with a-type flanking folds associated with a reverse
182 drag along the interboudin surface (Grasemann and Stüwe, 2001; Goscomb and Passchier, 2003).
183 Although the process has many similarities with the progressive development of flanking structures, the

184 major difference is that the interboudin surface (in contrast to cross-cutting elements of flanking
185 structures) terminates at the intersection between the interboudin surface and the boundary between
186 the boudinaged layer and the host rock. A major consequence of this confined slip along the interboudin
187 surface is a viscosity ratio-dependent rotation and deformation of the boudin segments (Dabrowski and
188 Grasemann, 2014). High viscosity ratios between the boudinaged layer and the host rock result in
189 rotation and tilting of almost rigid boudin segments, leading to bookshelf or domino boudinage (Ramsay
190 and Huber, 1987; Hanmer and Passchier, 1991). However, low viscosity ratios lead to rotation of both
191 the interboudin surface and the boudin block into the shear direction at different rates and strong
192 internal deformation of the individual boudin blocks. Figure 4 shows a numerical model (see Appendix
193 A.3. for model details) of the progressive formation of deformable domino boudins with periodic velocity
194 boundary conditions corresponding to an almost ideal dextral simple shear (a small amount of layer-
195 parallel extension is used to facilitate rotation of the boudin segments). The pre-defined aspect ratio of
196 the boudins is three and the initial interboudin surface is perpendicular to layering. Because this process
197 has many similarities with the formation of extensional antithetic flanking structures (compare with field
198 +III in Figs. 1 and 2b), which are associated with a marked reverse drag of central marker lines, several
199 studies on boudinage and flanking structures speculated that deformable domino boudinage may also
200 develop reverse drag of internal markers within the boudins (e.g. Grasemann and Stüwe, 1999; Passchier
201 and Druguet, 2002; Goscomb et al., 2004). Interestingly, our numerical model demonstrates that
202 mechanical layering has a strong influence on drag development along the interboudin surface and,
203 contrary to the expectation of previous studies, a marked normal drag develops within the boudins along
204 the interboudin surfaces, whereas reverse drag is only confined to the edge, where the interboudin
205 surface is in contact with the matrix (as highlighted by the arrow in Fig. 4c). Importantly, this marked
206 normal drag within the boudins along the antithetic and co-rotating interboudin surfaces resembles
207 boudin geometries that are mirror-symmetric to shear band boudinage developing under shear flow
208 with the opposite directions. In natural rocks, shear band boudins might be very difficult to discriminate
209 from deformable bookshelf boudins and should not be used as independent kinematic indicators without
210 constraints from other shear sense criteria.

211 2.3. Winged inclusions

212 Numerous studies have investigated the mechanical behaviour of inclusions such as porphyroclasts in
213 deformed rocks because they provide important information about the rheology, the properties of the
214 inclusion-matrix interface, the finite deformation and the flow kinematics (e.g. Mancktelow 2013;
215 Marques et al., 2014 and references cited therein). Such inclusions comprise single crystals (naked clasts,

216 mineral fish), porphyroclast systems (mantled porphyroclasts, porphyroclasts with reaction rims or strain
217 shadows), sigmoids (polycrystals) or winged inclusions, which are in general inclusions revealing a pinch-
218 and-swell geometry (Hanmer and Passchier, 1991; Passchier and Trouw, 2005). Dependent on a number
219 of possibly time-dependent factors, like mantle thickness, initial clast shape and orientation, clast-matrix
220 coupling, the clast-rim-matrix system's rheology, flow vorticity and finite strain, the porphyroclast
221 systems can develop σ -type or δ -type shapes with monoclinic symmetry that can serve as shear sense
222 indicators. σ -type inclusions can be furthermore classified into σ_a - and σ_b -types, with wings parallel to
223 the shear plane and to the synthetic shear bands, respectively (Passchier and Simpson, 1986).

224 Reworking of an isolated pinch-and-swell object by shear flow leads to the formation of a winged
225 inclusion (Hanmer, 1990). In contrast to σ_a - and σ_b -types clasts, where the wings develop a fixed position
226 on both sides of the clast and only the core is rotating, both the core and the wings of winged inclusions
227 rotate, although at different rates (Grasemann and Dabrowski, 2015). After the elongated core of winged
228 inclusions has rotated out of the shear plane to an inclined orientation, with the long axis of the
229 elongated core dipping shallowly into the shear direction (Fig. 5b), the resulting geometry can be easily
230 confused with σ_b -type clasts developing under an oppositely directed shear flow. With the wing ends still
231 attached to the central reference line the inclusions resemble the geometries of σ_b -type clasts, whose
232 wings are however oriented in a c' -orientation with an opposite shear sense. With further rotation (Fig.
233 5d), the wings rotate out of the central reference line resembling a stair-stepping geometry that would
234 yield the opposite shear sense if 'classically interpreted' (Passchier and Trouw, 2005). After a 180°
235 rotation of the core of the object, the wings, which rotate slower than the core, are stretched but still
236 inclined at a small angle against the shear direction (Fig. 5e). Clearly, σ_b -type clasts are difficult to
237 distinguish from winged inclusions developing under an opposite shear flow, in particular when the
238 orientation of the central reference line is not exactly known. However, a closer inspection of the
239 coupling between the clast and the matrix (Schmid and Podladchikov, 2005) and the presence of strongly
240 recrystallized material in the wings might help to distinguish between σ_b -type clast (decoupled) and
241 winged inclusions (coupled).

242 3. Discussion

243 3.1. Interpretation of selected natural examples.

244 The structure shown in Figure 6a formed in Middle Cretaceous clay-rich limestones of the Nahr Umr
245 Formation (Jabal Akhdar dome, Oman; picture courtesy of A. Grobe). A classical kinematic interpretation
246 of the structure would most likely yield shear band (foliation) boudinage with a top-to-the SW shear

247 sense. However, the overall shear sense is top-to-the NE, a sense confirmed by both regional tectonics
248 and other independent shear sense criteria (Grobe et al., in press). A closer inspection reveals that the
249 central marker layer (black solid line in Fig. 6a) exhibits normal drag along the cross-cutting elements
250 represented by secondary shear zones (orange dotted lines in Fig. 6a). With reference to the numerically
251 modelled geometry shown in Figure 4, we suggest that this structure developed as a deformable domino
252 boudinage within a layer having a low competence contrast with the host rocks, followed by subsequent
253 rotation of the interboudin surfaces into the shear directions producing antithetic slip but normal drag.

254 Figure 6b shows a polished slab from a loose marble mylonite block collected from the Brenner Mesozoic
255 of the Ötztal-Bundschuh Nappe System (Eastern Alps, Austria). The mylonites define a nappe boundary
256 and are thought to have formed during Cretaceous exhumation with a consistent top-to-the ESE shear
257 sense (Fügenschuh et al., 1997). Although it is tempting to interpret the structure as an asymmetric
258 shear band boudinage recording a top-to-the left shear sense, the sample has been sheared top-to-the
259 right, consistent with mm-sized mica-fish within impure layers located at the bottom, within and on top
260 of the boudinaged layer (arrows in Fig. 6b). In fact the structure can be best explained by early brittle
261 fractures that later developed into antithetic secondary shear zones during rotation into the shear
262 direction forming a system of parallel and conjugate flanking structures (Exner et al., 2006). Faults
263 dipping steeply into the shear direction were probably not rotated and hence record very little offset. On
264 the other hand, secondary shear zones with up to c. 1 cm antithetic offset rotated into the shear
265 direction. Note that the displacement profiles of the shear zones are rather flat (e.g., the displacement is
266 constant along zones labelled d_1 and d_2 in Fig. 6b) with high displacement gradients being restricted to
267 near the tips of shear zones, which sole into a phyllosilicate-rich layer within which displacement is
268 accommodated by contiguous sliding. This displacement transfer could explain the minor drag of marker
269 lines along the shear zones. This example illustrates that, although isolated flanking structures are quite
270 ambiguous shear sense criteria, a system of conjugate flanking structures exhibiting a triclinic symmetry
271 can unequivocally record the flow kinematics when carefully inspected.

272 Figure 6c shows conglomeratic calcschists of the Glockner-Nappe System (Wasserfallwinkel,
273 Großglockner). The deformed marble pebble exhibits well-developed wings with stair stepping,
274 suggesting a top-to-the SSE shear sense. However, regional structural observations (Kurz et al., 1996)
275 and SC-fabrics defined by shape preferred orientations of calcite grains observed at local outcrops
276 indicate an overall top-to-the NNW shear sense. We therefore propose that the structure is a winged
277 inclusion that formed by co-rotation of an elongated marble clast revolving by at least 180° so that the
278 kinematics is consistent with a top-to-the NNW shear sense. A comparison of this structure with

279 numerical modelling results (see Fig. 5e and Grasemann and Dabrowski, 2015) suggests that a core
280 rotation together with a switch of the right- and left-side wing is indicative of a high shear strain of $\gamma > 20$
281 (compare with Fig. 5e).

282 The flanking structure shown in Figure 6d is from an impure marble mylonite (N Kea, Greece). Marker
283 lines (black solid lines) exhibit a marked change from reverse to normal drag along a secondary shear
284 zone (red dotted line). This structure could be either interpreted as an antithetic flanking fold or as a
285 synthetic shear band, which would be consistent with the overall top-to-the SW shear sense observed
286 elsewhere. Comparison of the natural structure in Figure 6d with the modelled geometry shown in
287 Figure 2a indicates that the structure is indeed a synthetic shear band that developed under top-to-the
288 SW general shear on the basis of the following criteria: (i) A large displacement on the secondary shear
289 zone with marker lines exhibiting normal drag that is almost parallel to the secondary shear zone within
290 the extensional quadrants, where markers of the opposite (compressional) quadrants meet at very high
291 angles. (ii) A central marker line with pronounced normal drag that is not a hook-shape superposed on a
292 reverse drag, a typical feature for antithetic slip on secondary shear zones. (iii) High-angle fractures
293 rotated towards the SW just below the secondary shear zone (white arrows in Fig. 6d).

294 3.2. Discussion of selected published examples

295 The purpose of this section is a discussion of published kinematic indicators, which can be alternatively
296 interpreted, demonstrating that the examples displayed in Figure 6 are not unique or rare structures
297 developing under exceptional conditions, but are common phenomena in natural sheared rocks. We
298 emphasize that it is not our intention to question the published analysis but to discuss alternative
299 interpretations from the selected references

300 Ceccato et al. (2017) investigated texture inheritance during mylonitization of quartz veins within the
301 Rieserferner pluton, which underwent deformation during post-magmatic cooling at temperatures of
302 around 450 °C. The authors describe lenticular to fish-shaped ribbon porphyroclasts exhibiting stair-
303 stepping geometries climbing against the otherwise well-constrained shear sense, which is opposite to
304 that commonly observed in mica-fish within quartz mylonites (figure 10 in Ceccato et al., 2017). The
305 authors' explanation for the clast geometry is boudinage along micro-shear bands followed by co-
306 rotation of the ribbon porphyroclasts. Although this model would require that counter-rotation of the
307 clasts during shear-band boudinage is followed by co-rotation, this model is perfectly in line with the
308 development of winged inclusions of isolated lenticular-shaped grains coupled with the very fine-
309 recrystallized quartz matrix. The fish-shaped ribbon porphyroclasts of Ceccato et al. (2018) are strikingly

310 similar to quartz porphyroclasts with pinch-and-swell geometries from mylonitized quartz veins
311 occurring in the Schober Group in Austria (fig. 3e in Grasemann and Dabrowski, 2015) where the ‘non-
312 sense’ geometry has been explained by clast rotation into the shear direction resulting in winged
313 inclusions forming under a shear sense consistent with both the texture and the SC fabric within the
314 quartz mylonites (compare Fig. 5b).

315 In a review paper, Burg (1999) presents geometric and scale-invariant concepts applied to tectonic
316 studies of ductile structures. As an example for anastomosing shear zones in a bulk shear regime, the
317 author shows a spectacular example of an isolated asymmetric boudin within sheared amphibolites of
318 the Bulgarian Rhodope Massif (fig. 12 in Burg, 1999). The boudin has a prominent pinch-and-swell
319 geometry, which is, if the boudin is coupled to the host rock, inherently unstable during shear flow. We
320 propose that the structure could be in fact a winged inclusion (rather than an asymmetric boudin) on the
321 basis of the following two key observations, which can be explained by the core’s rotation and host rock
322 coupling (compare Fig. 5b and fig. 9 in Grasemann and Dabrowski, 2015): (i) Strain localization in the
323 form of shear zones along the shortening quadrants of the object and the attached wings and (ii) folding
324 in close vicinity of the object’s core in the extensional quadrants. The kinematic direction of the flow
325 suggested by the winged inclusion interpretation is furthermore supported by veins, which have been
326 boudinaged and rotated into the shear direction (lower right part of fig. 12 in Burg, 1999).

327 Following the collision of India and Asia, the subducted High Himalayan Crystalline extruded in
328 Miocene times between the Main Central Thrust at the base and the South Tibetan Detachment system
329 at the top (e.g. Hodges et al., 1996). Finch et al. (2014) investigated in detail the timing of shear sense
330 reversal at the top of the High Himalayan Crystalline and propose that mafic lithons within a migmatic
331 orthogneiss preserve reverse shearing. Their figure 5D shows K-feldspar porphyroblasts with asymmetric
332 tails resembling, at a first glance, σ_b -type clasts. This interpretation would however require either a back-
333 rotation of the clast, probably associated with decoupling of the clast-matrix system (Mancktelow et al.,
334 2002) or wing development along a C' -plane or synthetic shear band orientation (Passchier and Simpson,
335 1986). An alternative interpretation is that the structures represent winged inclusions that rotated into
336 the shear direction with a normal shear sense at the top of the High Himalayan Crystalline (compare with
337 Fig. 5c). This interpretation is in fact consistent with several σ_a -type clasts exhibiting clear stair stepping,
338 as shown in figure 5D of Finch et al. (2014).

339 Syros Island is part of the Cycladic blueschist belt (Greece) and experienced an Eocene high-
340 pressure metamorphism followed by an Oligocene/Miocene greenschist facies event. Various kinematic

341 interpretations, derived from different outcrops, but mainly on the basis of asymmetric boudinage, exist
342 in the literature for both events with a clear predominance of top-to-the E to NE directed shearing (see
343 Laurent et al., 2016 and references cited therein). On the basis of microstructures and several
344 macroscopic shear sense criteria, such as shear band boudinage and sigmoids with clear stair stepping
345 geometries in dolomite layers, Rogowitz et al. (2015) suggest a top-to-the W shear sense for the Eocene
346 event in some western parts of Syros. In contrast, Bond et al. (2007) report for the same outcrops a top-
347 to-the E shear sense based on boudinaged dolomite layers with monoclinic symmetries. However, their
348 described structure could also represent a sheared domino boudinage with low viscosity ratio (compare
349 their figure 5e with the numerical results shown in Fig. 4b), which would make it consistent with a top-
350 to-the W shear sense, as suggested by Rogowitz et al. (2015). An additional indicator for a low viscosity
351 ratio between the dolomite layers and the calcite host rock during deformation is pinch-and-swelling and
352 fish-mouth boudinage of dolomite layers (fig. 5e in Bond et al., 2007). Further, Bond et al. (2007) point
353 out that both (asymmetric) shear band boudinage and symmetric boudinage with orthorhombic
354 symmetry occur in the same outcrop (their figure 5e). This conundrum could be solved if the shear band
355 boudinage in the dolomite layer is interpreted as a set of fractures that developed a preferred
356 orientation ‘by chance’ under local coaxial flow conditions (see Fig. 3 and Schöpfer et al. 2017).

357 The internal zone of the Hellenides is generally considered to correlate with the Attic-Cycladic
358 metamorphic complex. Scheffer et al. (2016) investigated the syn- to post-orogenic western border of
359 the Attic-Cycladic metamorphic complex and concluded that the dominant top-to-the SSW and the local
360 top-to-the NNE shear sense are consistent with the area’s location at the junction between the bivergent
361 North and West Cycladic Detachments systems. Their figure 7b shows a calcite marble with a mylonitic
362 foliation wrapping around an ellipsoidal dolomite clast. Decoupling of the dolomite from the matrix
363 calcite and back-rotation of the clast into a stable position with the long axis inclined against the shear
364 directions would support the suggested local top-to-the NNE shear sense. An alternative, and in our view
365 more plausible, explanation for this ‘non-sense’ geometry however is instability of an ellipsoidal clast
366 with a strong matrix coupling and co-rotation out of the shear plane (compare with Fig. 5b and d), so
367 that the structure is consistent with the dominant top-to-the SSW shear sense reported elsewhere in the
368 area (Scheffer et al., 2016).

369 4. Conclusions

370 We have shown that there is a range of structures that ‘mimic’ well-established kinematic indicators with
371 the opposite shear sense, which may result, when ‘classically interpreted’, in wrong kinematic

372 interpretations. In particular the rotation of and slip on secondary shear zones and interboudin surfaces
373 of boudinaged layers with low-competence contrast result in structures that have to be interpreted
374 cautiously, especially if the deformation was under general shear flow. Furthermore, the rotation of
375 pinch-and-swell objects may result in geometries that are similar but mirror shapes of σ -type clasts or
376 sigmoids. We do not question the general applicability and success of classical interpretations of these
377 kinematic indicators, especially when the interpretations are conclusive and tested independently by
378 different criteria. However, shear sense observations that are in conflict with regional observations
379 should be carefully investigated and tested with mechanical models before local observations are
380 extrapolated to large-scale tectonics.

381 Acknowledgement

382 Fruitful discussions with C. Scheffer, J. Urai, A. Ceccato, A.H.N. Rice, A. Rogowitz and J. White are
383 gratefully acknowledged. A big thank you to A. Grobe for providing the picture and important
384 background information of Figure 6a. We thank the Austrian Academy of Sciences (Emil Suess-Erbschaft)
385 for financial support for field work. Editorial handling of the manuscript by Cees Passchier is gratefully
386 acknowledged. The manuscript was improved by constructive reviews by Stefan Schmalholz and an
387 anonymous reviewer.

388 References

- 389 Abe, S., van Gent, H., Urai, J. L., 2011. DEM simulation of normal faults in cohesive materials.
390 *Tectonophysics* 512, 12-21.
- 391 Adamuszek, M., Dabrowski, M., 2017. Sheath fold development in monoclinic shear zones. *Terra Nova*
392 29, 356-362.
- 393 Behrmann, J.H., 1987. A precautionary note on shear bands as kinematic indicators. *J. Struct. Geol.* 9,
394 659-666.
- 395 Berthé, D., Choukroune, P., Jegouzo, P., 1979. Orthogneiss, mylonite and non coaxial deformation of
396 granites: the example of the South Armorican shear zone. *J. Struct. Geol.* 1, 31-43.
- 397 Billings, M.P., 1972. *Structural Geology*, 3rd ed. ed. Prentice-Hall, Englewood Cliffs, NJ, 606 pp.
- 398 Blenkinsop, T.G., 2000. *Deformation Microstructures and Mechanisms in Minerals and Rocks*. Kluwer
399 Academic Publisher, Dordrecht, 150 pp.
- 400 Bond, C.E., Butler, R.W.H., Dixon, J.E., 2007. Co-axial horizontal stretching within extending orogens: the
401 exhumation of HP rocks on Syros (Cyclades) revisited. *Geol. Soc. Spec. Publ.* 272, 203-222.

402 Burg, J.-P., 1999. Ductile structures and instabilities: their implication for Variscan tectonics in the
403 Ardennes. *Tectonophysics* 309, 1-25.

404 Ceccato, A., Pennacchioni, G., Menegon, L., Bestmann, M., 2017. Crystallographic control and texture
405 inheritance during mylonitization of coarse grained quartz veins. *Lithos* 290-291, 210-227.

406 Coelho, S., Passchier, C., Grasemann, B., 2005. Geometric description of flanking structures. *J. Struct.
407 Geol.* 27, 597-606.

408 Dabrowski, M., Krotkiewski, M., Schmid, D.W., 2008. MILAMIN: MATLAB-based finite element method
409 solver for large problems. *Geochem. Geophys. Geosyst.* 9, Q04030, doi:10.1029/2007GC001719

410 Dabrowski, M., Schmid, D.W., 2011. A rigid circular inclusion in an anisotropic host subject to simple
411 shear. *J. Struct. Geol.* 33, 1169-1177.

412 Dabrowski, M., Grasemann, B., 2014. Domino boudinage under layer-parallel simple shear. *J. Struct.
413 Geol.* 68, Part A, 58-65.

414 De Paor, D.G., Means, W.D., 1984. Mohr circles of the First and Second Kind and their use to represent
415 tensor operations. *J. Struct. Geol.* 6, 693-701.

416 de Sitter, L.U., 1964. *Structural geology*, 2nd Edition ed. McGraw-Hill Inc., New York, 551 pp.

417 Elliott, D., 1972. Deformation Paths in Structural Geology. *Geol. Soc. Am. Bull.* 83, 2621-2638.

418 Eshelby, J.D., 1959. The elastic field outside an ellipsoidal inclusion. *Proc. Royal Soc. A*, 252 561-569.

419 Exner, U., Mancktelow, N.S., Grasemann, B., 2004. Progressive development of s-type flanking folds in
420 simple shear. *J. Struct. Geol.* 26, 2191-2201.

421 Exner, U., Grasemann, B., Mancktelow, N.S., 2006. Multiple faults in ductile simple shear: analogue
422 models of flanking structure systems. *Geol. Soc. Lond., Special Publications* 253, 381-395.

423 Exner, U., Dabrowski, M., 2010. Monoclinic and triclinic 3D flanking structures around elliptical cracks. *J.
424 Struct. Geol.* 32, 2009-2021.

425 Fairbairn, H.W., 1949. *Structural petrology of deformed rocks*, 2nd edition ed. Addison-Wesley Press Inc.,
426 Cambridge, 344 pp.

427 Finch, M., Hasalová, P., Weinberg, R.F., Fanning, C.M., 2014. Switch from thrusting to normal shearing in
428 the Zaskar shear zone, NW Himalaya: Implications for channel flow. *Geol. Soc. Am. Bull.* 126, 892-924.

429 Fletcher, R.C., 2009. Deformable, rigid, and inviscid elliptical inclusions in a homogeneous incompressible
430 anisotropic viscous fluid. *J. Struct. Geol.* 31, 382-387.

431 Fossen, H., 2016. *Structural Geology*, 2nd Edition ed. Cambridge University Press, 524 pp.

432 Fügenschuh, B., Seward, D., Mancktelow, N., 1997. Exhumation in a convergent orogen: the western
433 Tauern window. *Terra Nova* 9, 213-217.

434 Ghosh, S.K., Ramberg, H., 1976. Reorientation of inclusions by combination of pure and simple shear.
435 *Tectonophysics* 34, 1-70.

436 Goscombe, B.D., Passchier, C.W., 2003. Asymmetric boudins as shear sense indicators--an assessment
437 from field data. *J. Struct. Geol.* 25, 575-589.

438 Goscombe, B.D., Passchier, C.W., Hand, M., 2004. Boudinage classification: end-member boudin types
439 and modified boudin structures. *J. Struct. Geol.* 26, 739-763.

440 Grasemann, B., Stüwe, K., 2001. The development of flanking folds during simple shear and their use as
441 kinematic indicators. *J. Struct. Geol.* 23, 715-724.

442 Grasemann, B., Stüwe, K., Vannay, J.-C., 2003. Sense and non-sense of shear in flanking structures. *J.*
443 *Struct. Geol.* 25, 19-34.

444 Grasemann, B., Martel, S., Passchier, C., 2005. Reverse and normal drag along a fault. *J. Struct. Geol.* 27,
445 999-1010.

446 Grasemann, B., Dabrowski, M., 2015. Winged inclusions: Pinch-and-swell objects during high-strain
447 simple shear. *J. Struct. Geol.* 70, 78-94.

448 Grobe, A., Virgo, S., von Hagke, C., Urai, J. L., Littke, R., in press. Multiphase structural evolution of a
449 continental margin during obduction orogeny: Insights from the Jebel Akhdar Dome, Oman Mountains.
450 *Tectonics*.

451 Hanmer, S., 1990. Natural rotated inclusions in non-ideal shear. *Tectonophysics* 176, 245-255.

452 Hanmer, S., Passchier, C.W., 1991. Shear sense indicators: a review. Paper – *Geol. Surv. Canada* 90, 1-71.

453 Hills, E.S., 1972. *Elements of Structural Geology*. Methuen and Co., London, 502 pp.

454 Hodges, K.V., Parrish, R.R., Searle, M.P., 1996. Tectonic evolution of the central Annapurna Range,
455 Nepalese Himalayas. *Tectonics* 15, 1264-1291.

456 Hudleston, P.J., 1989. The association of folds and veins in shear zones. *J. Struct. Geol.* 11, 949-957.

457 Jiang, D., 2007. Numerical modeling of the motion of rigid ellipsoidal objects in slow viscous flows: A new
458 approach. *J. Struct. Geol.* 29, 189-200.

459 Kocher, T., Mancktelow, N.S., 2005. Dynamic reverse modelling of flanking structures: a source of
460 quantitative kinematic information. *J. Struct. Geol.* 27, 1346-1354

461 Kurz, W., Neubauer, F., Genser, J., 1996. Kinematics of Penninic nappes (Glockner Nappe and basement-
462 cover nappes) in the Tauern Window (Eastern Alps, Austria) during subduction and Penninic-
463 Austroalpine collision. *Eclogae Geol. Helv.* 89, 573-605.

464 Laurent, V., Jolivet, L., Roche, V., Augier, R., Scaillet, S., Cardello, G.L., 2016. Strain localization in a
465 fossilized subduction channel: Insights from the Cycladic Blueschist Unit (Syros, Greece). *Tectonophysics*
466 672–673, 150-169.

467 Lister, G.S., Williams, P.F., 1979. Fabric development in shear zones: theoretical controls and observed
468 phenomena. *J. Struct. Geol.* 1, 283-297.

469 Mancktelow, N.S., Arbaret, L., Pennacchioni, G., 2002. Experimental observations on the effect of
470 interface slip on rotation and stabilisation of rigid particles in simple shear and a comparison with natural
471 mylonites. *J. Struct. Geol.* 24, 567-585.

472 Mancktelow, N.S., 2008. Tectonic pressure: Theoretical concepts and modelled examples. *Lithos* 103,
473 149-177.

474 Mancktelow, N.S., 2013. Behaviour of an isolated rimmed elliptical inclusion in 2D slow incompressible
475 viscous flow. *J. Struct. Geol.* 46, 235-254.

476 Mandal, N., Kumar Samanta, S., Chakraborty, C., 2000a. Progressive development of mantle structures
477 around elongate porphyroclasts: insights from numerical models. *J. Struct. Geol.* 22, 993-1008.

478 Mandal, N., Chakraborty, C., Samanta, S.K., 2000b. Boudinage in multilayered rocks under layer-normal
479 compression: a theoretical analysis. *J. Struct. Geol.* 22, 373-382.

480 Mandal, N., Dhar, R., Misra, S., Chakraborty, C., 2007. Use of boudinaged rigid objects as a strain gauge:
481 Insights from analogue and numerical models. *J. Struct. Geol.* 29, 759-773.

482 Marques, F.O., Mandal, N., Taborda, R., Antunes, J.V., Bose, S., 2014. The behaviour of deformable and
483 non-deformable inclusions in viscous flow. *Earth-Sci. Rev.* 134, 16-69.

484 Means, W.D., Hobbs, B.E., Lister, G.S., Williams, P.F., 1980. Vorticity and non-coaxiality in progressive
485 deformation. *J. Struct. Geol.* 2, 371-378.

486 Mulchrone, K.F., Grogan, S., De, P., 2005. The relationship between magmatic tiling, fluid flow and crystal
487 fraction. *J. Struct. Geol.* 27, 179.

488 Passchier, C.W., 1986. Flow in natural shear zones - the consequences of spinning flow regimes. *Earth
489 Planet Sci. Lett.* 77, 70-80.

490 Passchier, C.W., Simpson, C., 1986. Porphyroclast systems as kinematic indicators. *J. Struct. Geol.* 8, 831-
491 844.

492 Passchier, C.W., 1988. Analysis of deformation paths in shear zones. *Geol. Rundsch.* 77, 309-318.

493 Passchier, C.W., Williams, P.R., 1996. Conflicting shear sense indicators in shear zones; the problem of
494 non-ideal sections. *J. Struct. Geol.* 18, 1281-1284.

495 Passchier, C.W., 2001. Flanking structures. *J. Struct. Geol.* 23, 951-962.

496 Passchier, C.W., Druguet, E., 2002. Numerical modelling of asymmetric boudinage. *J. Struct. Geol.* 24,
497 1789-1803.

498 Passchier, C.W., Trouw, R.A.J., 2005. *Microtectonics*, 2nd, Revised and Enlarged ed. Springer-Verlag,
499 Berlin, 366 pp.

500 Petit, J.P., 1987. Criteria for the sense of movement on fault surfaces in brittle rocks. *J. Struct. Geol.* 9,
501 597-608.

502 Platt, J.P., Vissers, R.L.M., 1980. Extensional structures in anisotropic rocks. *J. Struct. Geol.* 2, 397-410.

503 Potyondy, D.O., Cundall, P.A., 2004. A bonded-particle model for rock. *Int. J. Rock Mech. Min. Sci.* 41,
504 1329-1364.

505 Ramberg, H., 1975. Particle paths, displacement and progressive strain applicable to rocks.
506 *Tectonophysics* 28, 1-37.

507 Ramsay, J.G., Huber, I.M., 1987. The Techniques of Modern Structural Geology. Volume 2: Folds and
508 Fractures. Academic Press Inc. Ltd, London. 309-700.

509 Rogowitz, A., Huet, B., Schneider, D., Grasemann, B., 2015. Influence of high strain rate deformation on
510 ⁴⁰Ar/³⁹Ar mica ages from marble mylonites (Syros, Greece). *Lithosphere* 7, 535-540.

511 Samanta, S.K., Mandal, N., Chakraborty, C., 2002. Development of structures under the influence of
512 heterogeneous flow field around rigid inclusions: insights from theoretical and numerical models. *Earth-*
513 *Sci. Rev.* 58, 85-119.

514 Sander, B., 1950. Einführung in die Gefügekunde der geologischen Körper: Zweiter Teil: Die Korngefüge.
515 Springer-Verlag Berlin Heidelberg, Wien, 338 pp.

516 Scheffer, C., Vanderhaeghe, O., Lanari, P., Tarantola, A., Ponthus, L., Photiades, A., France, L., 2016. Syn-
517 to post-orogenic exhumation of metamorphic nappes: Structure and thermobarometry of the western
518 Attic-Cycladic metamorphic complex (Lavrion, Greece). *J. Geodyn.* 96, 174-193.

519 Schenk, O., Urai, J. L., van der Zee, W., 2007. Evolution of boudins under progressively decreasing pore
520 pressure A case study of pegmatites enclosed in marble deforming at high grade metamorphic
521 conditions, Naxos, Greece. *Am. J. Sci.* 307, 1009-1033.

522 Schmalholz, S.M., Maeder, X., 2012. Pinch-and-swell structure and shear zones in viscoplastic layers. *J.*
523 *Struct. Geol.* 37, 75-88.

524 Schmid, D.W., Podladchikov, Y.Y., 2004. Are isolated stable rigid clasts in shear zones equivalent to
525 voids? *Tectonophysics* 384, 233-242.

526 Schmid, D.W., Podladchikov, Y.Y., 2005. Mantled porphyroclast gauges. *Journal of Structural Geology* 27,
527 571-585.

528 Schöpfer, M.P.J., Childs, C., Manzocchi, T., Walsh, J.J., Nicol, A., Grasemann, B., 2017. The emergence of
529 asymmetric normal fault systems under symmetric boundary conditions. *J. Struct. Geol.* 104, 159-171.

530 Simpson, C., Schmid, S.M., 1983. An evaluation of criteria to deduce the sense of movement in sheared
531 rocks. *Geol. Soc. Am. Bull.* 94, 1281-1288.

532 Strömgård, K.E., 1973. Stress distribution during deformation of boudinage and pressure shadows.
533 *Tectonophysics* 16, 215-248.

534 Turner, F.J., Weiss, L.E., 1963. Structural analysis of metamorphic tectonites. McGraw-Hill, New York,
535 1963.

536 Twiss, R.J., Moores, E.M., 2007. Structural Geology, 2nd Edition ed. W.H. Freeman and Company, New
537 York, 736 pp.

538 van der Pluijm, B., Marshak, S., 2004. Earth Structure - an Introduction to Structural Geology and
539 Tectonics, Second Edition ed. W. W. Norton & Company, New York. 672 pp.

540 White, S.H., 1979. Large strain deformation: report on a Tectonic Studies Group discussion meeting held
541 at Imperial College, London on 14 November 1979. *J. Struct. Geol.* 1, 333-339.

542 White, S.H., Bretan, P.G., Rutter, E.H., 1986. Fault zone reactivation: kinematics and mechanisms. *Philos.*
543 *Trans. R. Soc. Lond. A-317*, 81-97.

544 Wiesmayr, G., Grasemann, B., 2005. Sense and non-sense of shear in flanking structures with layer-
545 parallel shortening: implications for fault-related folds. *J. Struct. Geol.* 27, 249-264.

546 Xypolias, P., 2010. Vorticity analysis in shear zones: A review of methods and applications. *J. Struct. Geol.*
547 32, 2072-2092.

548

549 Figure Captions

550 Figure 1: Physical space and off-axis Mohr circle (De Paor and Means, 1984) of the deformation gradient
551 tensor (F) showing the eigenvectors of flow ($a_{1,2}$), the angle α between the eigenvectors, the
552 instantaneous stretching axes ($ISA_{1,2}$), and the maximum and minimum shear strain rate ($\dot{\gamma}_{1,2}$). a) In
553 simple shear ($W_k = 1$) the instantaneous shear and stretch of a finite-length slip surface is characterized
554 by four different sectors, in which material lines are co-rotating: (+I) synthetic slip, shortening; (+II)
555 antithetic slip, shortening; (+III) antithetic slip, stretching; (+IV) synthetic slip, stretching. b) In general
556 shear ($W_k = 0.8$), two additional sectors are present and characterized by counter-rotation of material
557 lines: (-I) synthetic slip, shortening; (-II) synthetic slip, stretching.

558 Figure 2: Selected mechanical models (for model details see Appendix A.1.) of an inviscid slip surface (red
559 line) embedded in an incompressible viscous matrix showing the development of flanking structures
560 visualized by passive marker lines (central grey layer and black thin solid lines). Insets in the right corners
561 give the initial orientations of the slip surface. ψ - initial orientation of the slip surface with respect to the
562 shear direction; F – deformation gradient tensor; W_k – kinematic vorticity number. Half arrows indicate
563 the modelled shear sense (dextral shear is positive): The central marker line exhibits a) synthetic
564 extensional offset with normal drag, b) antithetic extensional offset with normal drag, c) contractional
565 antithetic offset, and d) contractional synthetic offset.

566 Figure 3: Results of three discrete element method (DEM) models (for model details see Appendix A.2.)
567 of the formation of fracture boudinage under coaxial strain boundary conditions comprising a brittle
568 layer (with passive markers) embedded in a weak matrix at 10% extension. The polarity of the fracture
569 system P is the normalized sum of throw on left dipping (positive) and right dipping (negative) fractures.
570 a) Dominant left-dipping interboudin surfaces. b) Almost no dominant dip direction. c) Dominant right-
571 dipping interboudin surfaces.

572 Figure 4: Finite elements method (FEM) models (for model details see Appendix A.3.) illustrating the
573 progressive deformation of domino boudins under a velocity boundary conditions close to dextral simple
574 shear ($W_k = 0.9998$). The initial aspect ratio of the boudins is three and the interboudin surfaces are
575 initially perpendicular to layering. F is the exact imposed deformation gradient tensor, but since the
576 deformation is very close to simple shear the stages shown correspond approximately to a shear strain
577 of a) $\gamma = 5$, b) $\gamma = 10$, and c) $\gamma = 15$. Note how the pronounced normal drag within the boudins along the
578 interboudin surfaces provides geometric similarities with asymmetric shear band boudinage forming
579 under the opposite shear sense. Only at the boudin edges, where the interboudin surfaces are in contact
580 with the matrix, reverse drag develops (white arrows).

581 Figure 5: FEM models (for model details see Appendix A.3.) of sinistral simple shearing of an isolated
582 object with initial pinch-and-swell geometry progressively developing into a winged inclusion at shear
583 strains of a) $\gamma = 0$, b) $\gamma = 5$, c) $\gamma = 10$, d) $\gamma = 15$, and e) $\gamma = 20$. The viscosity ratio between the object and
584 the matrix is 100. The dotted black line is a central reference line initially parallel to the shear plane.
585 Note that after $\gamma = 5$ and $\gamma = 20$ the winged inclusion resembles a σ_b -type clast with stair stepping
586 suggesting dextral shear sense.

587 Figure 6: Selected natural examples that are prone to be misinterpreted. a) Foliation boudinage in
588 Middle Cretaceous clay-rich limestones of the Nahr Umr Formation (Jabal Akhdar dome, Oman,
589 2583932N, 518009E, UTM40). The shear sense is top-to-the NE and confirmed by other independent
590 shear sense criteria (Grobe et al., in press). The central marker layer (black solid line) exhibits normal
591 drag along antithetic cross-cutting elements (orange dotted lines) similar to the numerical models shown
592 in Figure 4. Note that this structure could be easily misinterpreted as a shear band (foliation) boudinage
593 yielding a top-to-the SW shear sense (picture courtesy of A. Grobe). b) Loose marble mylonite block
594 collected from the Brenner Mesozoic of the Ötztal-Bundschuh Nappe System (Eastern Alps, Austria,
595 5216856N, 682297E, UTM32). Although it is tempting to interpret the structure as an asymmetric
596 boudinage with a top-to-the left shear sense, the sample was sheared top-to-the right, an interpretation
597 consistent with large mica-fish within impure marble layers (orange arrows). Note the low displacement
598 gradient along the interboudin surfaces characteristic for domino boudinage. c) Conglomeratic
599 calcschists of the Glockner-Nappe System (Wasserfallwinkel, Großglockner, 327568E, 5218286N,
600 UTM33). The deformed marble pebble exhibits a clear stair stepping suggesting a top-to-the SSE sense of
601 shear. However, the structure developed during co-rotation of an elongated marble clast with wings
602 slightly oblique to the main foliation. Note how the SC-fabric in the marble host rock is consistent with
603 the overall top-to-the NNW sense of shear recorded elsewhere (Kurz et al., 1996). d) Flanking structures

604 in an impure marble mylonite showing a noticeable change from reverse to normal drag of marker lines
605 (black solid lines) along a secondary shear zone (red dotted line). The structure could be interpreted as
606 an antithetic flanking fold or, alternatively and therefore consistent with an overall top to-the SW shear
607 sense, as a synthetic shear band (Outzia area, N Kea, Greece, 4173029N, 265213E, UTM35). The latter
608 interpretation is supported by high angle fractures rotated into the shear direction (white arrows).

609 DR 1: Movie of a mechanical model (for model details see Appendix A.1.) of an inviscid slip surface (red
610 line) embedded in an incompressible viscous matrix showing the progressive development of flanking
611 structures during ideal dextral simple shear. Initially the slip surface dips with 20° into the shear
612 direction. As the slip surface rotates into the shear direction, the offset on the slip surface is at first
613 synthetic. However, after reaching a dip of 45° into the shear direction, a shear sense reversal from syn-
614 to antithetic occurs and reverse drag antithetic flanking folds with a pronounced hook-shape develop.
615 Lastly, after a dip of 45° against the shear direction is reached, a shear sense reversal on the slip surface
616 from anti- to synthetic occurs.

617 Appendix

618 A.1. Eshelby

619 The modelling of flanking structures under general shear is performed using an approach similar to the
620 method described in Kocher and Mancktelow (2005). For any given far field flow conditions and the
621 current orientation of the cross-cutting element, the velocity field in the matrix is computed using the
622 semi-analytical solution implemented in MATLAB and described in Exner and Dabrowski (2010) and
623 Adamuszek and Dabrowski (2017). The cross-cutting element is modelled as a frictionless blade crack
624 embedded in an isotropic linear viscous matrix and the solution is based on a reduced version of the
625 external Eshelby solution (Eshelby, 1959), which accounts for both material incompressibility and an
626 elliptic rather than an ellipsoidal inviscid inclusion. The developing structures are tracked with a set of
627 initially horizontal material lines that are passively deformed by the evolving flow in the matrix. The lines'
628 advection is computed using a highly accurate numerical solver, namely `ode45` as implemented in
629 MATLAB (www.mathworks.com).

630 A.2. DEM

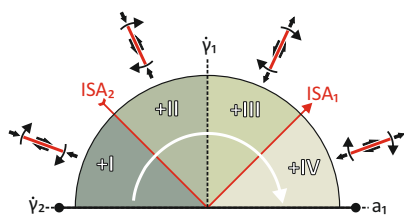
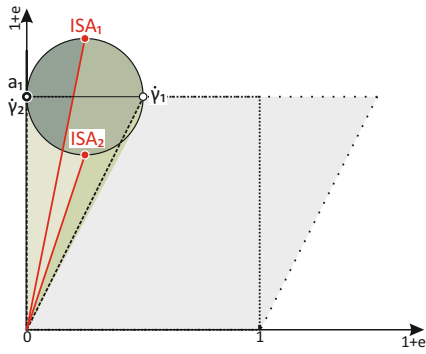
631 The Particle Flow Code in two dimensions (PFC-2D; Itasca Consulting Group, 2008), which implements
632 the Distinct Element Method (DEM) for circular particles (Potyondy and Cundall, 2004), is used to model
633 the formation of fracture boudinage developing in a central brittle layer embedded in a weak

634 (cohesionless) matrix under symmetric (coaxial strain) boundary conditions. The three models shown in
635 Fig. 3 are a selection from a total of 32 model realizations with identical particle/bond properties, but
636 different random placement of particles. Different fracture system geometries and polarities are hence a
637 result of small differences in the initial conditions, a characteristic feature of chaotic behavior. For model
638 details, statistical analyses and discussion see Schöpfer et al. (2017).

639 A.3. MILAMIN

640 MILAMIN (Dabrowski et al., 2008), a MATLAB (www.mathworks.com) implementation of the finite
641 element method, is used to compute the flow field in and around the deforming boudins and the pinch-
642 and-swell objects presented in this work (Figs. 4 and 5, respectively). An unstructured triangular
643 computational mesh, which is frequently regenerated to maintain its quality and to accurately describe
644 the progressive structural development, is used (for details see Dabrowski and Grasemann, 2014;
645 Grasemann and Dabrowski, 2015).

a) $D=[1 \ 0.5; 0 \ 1]$, $Wk=1$



b) $D=[1.5 \ 0.5; 0 \ 0.667]$, $Wk=0.8$

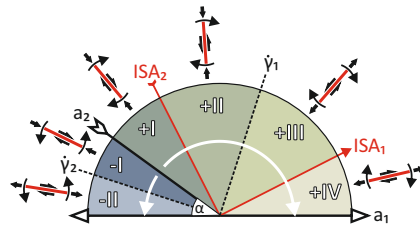
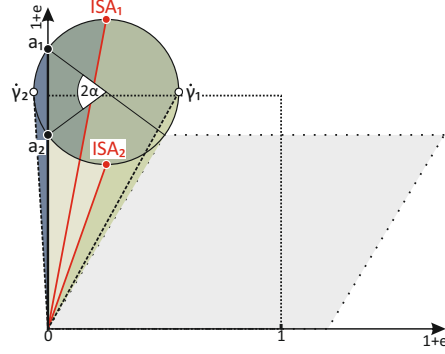


Fig. 1 - Grasmann et al JSG40

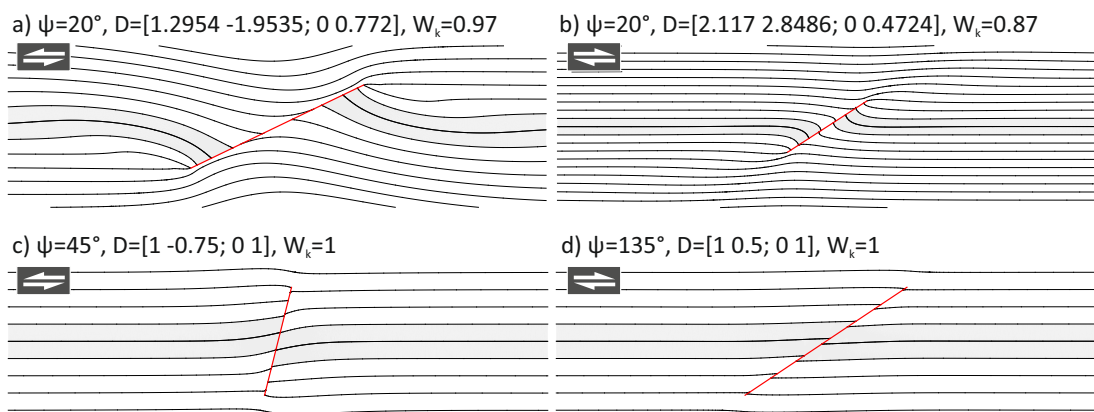


Fig. 2 - Grasmann et al JSG40

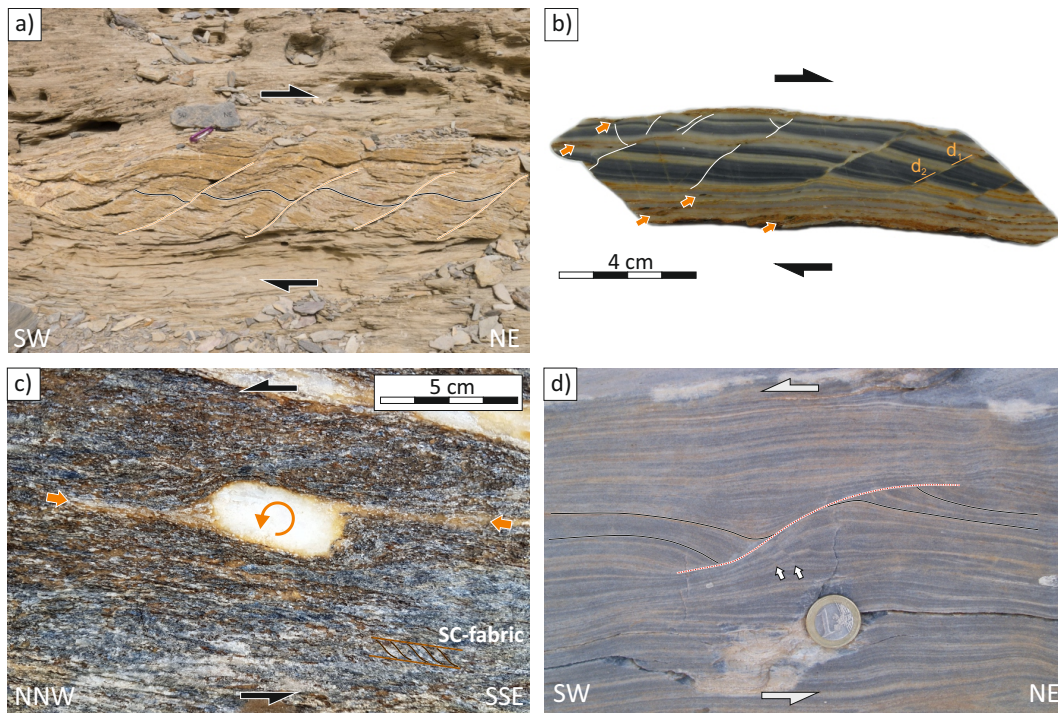


Fig. 6 - Grasmann et al JSG40